General Strategy for Fabricating Transparent TiO_2 Nanotube Arrays for Dye-Sensitized Photoelectrodes: Illumination Geometry and Transport Properties

Jin Young Kim,[†] Jun Hong Noh,[‡] Kai Zhu,[†] Adam F. Halverson,[†] Nathan R. Neale,[†] Sangbaek Park,[‡] Kug Sun Hong,[‡] and Arthur J. Frank[†,*]

[†]National Renewable Energy Laboratory, Golden, Colorado 80401-3393, United States, and [‡]Department of Materials Science and Engineering, Seoul National University, Seoul 151-744, Korea

ABSTRACT We report on the preparation of transparent oriented titania nanotube (NT) photoelectrodes and the effect of illumination direction on light harvesting, electron transport, and recombination in dye-sensitized solar cells (DSSCs) incorporating these electrodes. High solar conversion efficiency requires that the incident light enters the cell from the photoelectrode side. However, it has been synthetically challenging to prepare transparent TiO_2 NT electrodes by directly anodizing Ti metal films on transparent conducting oxide (TCO) substrates because of the difficulties of controlling the synthetic conditions. We describe a general synthetic strategy for fabricating transparent TiO_2 NT films on TCO substrates. With the aid of a conducting Nb-doped TiO_2 (NTO) layer between the Ti film and TCO substrate, the Ti film was anodized completely without degrading the TCO. The NTO layer was found to protect the TCO from degradation through a self-terminating mechanism by arresting the electric field-assisted dissolution process at the NT—NTO interface. The illumination direction and wavelength of the light incident on the DSSCs were shown to strongly influence the incident photon-to-current conversion efficiency, light-harvesting, and charge-collection properties, which, in turn, affect the photocurrent density, photovoltage, and solar energy conversion efficiency. Effects of NT film thickness on the properties and performance of DSSCs were also examined. Illuminating the cell from the photoelectrode substantially increased the conversion efficiency compared with illuminating it from the counter-electrode side.

KEYWORDS: transparent · TiO_2 nanotube · anodization · Nb-doped TiO_2 · dye-sensitized solar cells · illumination geometry · charge transport

Well-ordered arrays of one-dimensional semiconductors, such as titania nanotubes (NTs), have attracted attention as an electrode architecture for optoelectronic applications, such as solar energy conversion,[1−4] electrochromics,[5] luminescence,[6] and sensors.[7−9] A prominent example of the use of TiO_2 NT arrays for solar energy conversion is the dye-sensitized solar cell (DSSC; also known as the Grätzel cell).[10−13] The traditional DSSC features dye molecules chemisorbed onto the surface of a mesoporous TiO_2 nanoparticle (NP) film deposited onto a transparent conducting oxide (TCO) substrate. The TCO substrate collects electrons from the film and transmits them to the external circuit, where they reenter the cell at the counter electrode. The pores of the film are filled with a liquid electrolyte containing the triiodide/iodide redox couple. Normally, light enters the DSSC through the TCO substrate on which the NPs are deposited. When NP-based DSSCs are illuminated through the counter electrode, however, their conversion efficiencies drops by about 30% because the platinum catalyst on the surface of the counter electrode and redox species (I_3^-/I^-) in the liquid electrolyte attenuate a significant fraction of the photons in the visible spectrum.[14] The illumination geometry also influences other cell properties. For instance, photoinjected electrons generated near the outermost regions of the NP film, closest to the counter electrode, spend a longer time in the film before being collected at the TCO substrate than those produced closest to the TCO substrate. Because the collection of photoinjected electrons competes with recombination, the longer the electrons spend in the film, the higher the probability of their undergoing recombination before being collected.[15] The extent to which illumination geometry affects NT-based DSSCs is problematic, as light normally enters the cell through the counter electrode because a nontransparent titanium foil is typically used as the substrate for forming the aligned NTs and for making electrical contact with them. It is noteworthy that when both the NT- and NP-DSSCs are

* Address correspondence to Arthur.Frank@nrel.gov.

Received for review October 12, 2010 and accepted March 2, 2011.

Published online March 11, 2011
10.1021/nn200440u

© 2011 American Chemical Society

illuminated through the counter electrode, the NT cells display higher charge-collection and light-harvesting efficiencies.[16] The constraints of illumination only through the counter electrode also limit the use of the NT architecture in solid-state solar cells (*e.g.*, spiro-OMeTAD-based DSSCs,[17] quantum dot-based cells,[18,19] and hybrid organic−inorganic cells[20]) that require the hole-transmitting phase of the cell to be in electrical contact with a nontransparent silver or gold hole-collecting layer.

It has been challenging to prepare aligned TiO_2 NT arrays on TCO substrates because the synthesis generally relies on depositing a Ti film on a TCO substrate and then anodizing it at high positive potentials in a fluoride-containing electrolyte.[21] These conditions can lead to the degradation of the TCO and detachment of the NT film from the substrate. Two approaches have been developed to avoid this issue. In one approach, the NT arrays were prepared on a Ti foil followed by selective dissolution of the metal, leaving a freestanding NT layer that was physically transferred to a TCO substrate.[22] In the second approach, the anodization process was terminated before the Ti film was completely oxidized to titanium oxide, leaving a Ti layer between the NTs and TCO. Subsequent thermal annealing of the amorphous TiO_x NTs and Ti layer in air results in their becoming transparent.[23] The successful implementation of the latter approach required careful control of the synthesis conditions. Titanium films were deposited by sputtering either at high temperatures[21,24] or with an Ar-ion bombardment.[25] Generally, a second Ti layer was also deposited onto the first one to compensate for variations in the anodization (or etching) rate across the sample surface and to prevent short circuiting at the solution−air interface.[21,25] Terminating the anodization process too prematurely leaves a relatively thick Ti layer, which, when thermally annealed, results in a correspondingly insulating oxide layer that contributed to resistive losses in the DSSC. Depending on the thickness of the Ti layer and annealing temperature, a residual Ti might still remain. Annealing of TiO_2 NT films grown on a Ti substrate at temperatures $\geq$ 500 °C leads to the formation of rutile in the Ti substrate, which initiates the growth and propagation of the rutile crystallites in the anatase NT walls.[26,27] The growth of the rutile phase is found to cause the breakdown of the NT walls at temperatures approaching 600 °C.[26]

In this work, we describe a general strategy for fabricating transparent oriented TiO_2 NT electrodes. With the aid of a conducting Nb-doped TiO_2 (NTO) layer between the Ti film and TCO substrate, the Ti film can be anodized completely without harming the TCO and NT arrays, even after a prolonged anodization period. Annealing the as-deposited amorphous TiO_x NT films at temperatures as high as 590 °C produced only the TiO_2 anatase phase, substantiating the absence of the Ti metal layer after completion of the anodization process. The mechanism by which the NTO layer protects the NT film and TCO is discussed. The illumination direction (light incident from the electron collector side *versus* the counter-electrode side) is found to strongly influence the transport times of electrons, incident photon-to-current conversion efficiency (IPCE), and photoelectrochemical properties of the transparent TiO_2 NT-based DSSCs. The strategy for preparing transparent NT films on a transparent conducting substrate using the NTO layer is easy to apply and will find important usage for sensitized solar cells and other optoelectronic applications.

RESULTS AND DISCUSSION

Characterization of the Anodization Process and Film Morphology. The field-emission scanning electron microscopy (FE-SEM) image in Figure 1a displays the top view of an as-deposited film before ion-beam etching. As discussed below, a porous overlayer on the surface of the film obstructs the view of the NT structure. The inset in Figure 1a shows the surface topography of the Ti layer on top of the NTO film before anodization. The presence of an overlayer has been observed previously[28] and has been ascribed to the low etching rate of the oxide in the ethylene glycol used in the anodization process.[25] However, even when the ionic conductivity of the ethylene glycol was increased, the formation of the overlayer could not be prevented.[25] We find that a postgrowth ion-beam etching (1.2 keV, 26 mA, and 30 min) can remove the porous overlayer, revealing the distinct NT film architecture and the compact packing of the array (Figure 1b). Analysis of the magnified FE-SEM image (Figure 1b) shows that the average NT pore diameters, wall thicknesses, and center-to-center distances between NTs are roughly 56, 42, and 142 nm, respectively. From these parameters, we estimate[16] an average intertube spacing of 1 nm, a film porosity of 26%, and a roughness factor of 35.3 μm^{-1}. Figure 1c displays the cross-sectional FE-SEM image of an as-prepared 6.4 μm thick NT film. Consistent with the observations of others,[25] the as-prepared NT films (6.4 μm) were always thicker than the starting Ti films (2.4 μm). Moreover, we found that the ratio of the NT film thickness to the Ti film thickness (*ca.* 2.6−2.7) was approximately constant, independent of the thickness of the NT films. For instance, a 5 μm thick Ti film was also required to form a 13 μm thick NT film (Figure S1 in the Supporting Information). The individual NTs of the film are seen to be highly oriented and homogeneous across several tens of micrometers of the NTO/TCO substrate surface. Figure 1d shows a photograph of the as-deposited transparent NT film on a NTO/TCO substrate. Relatively large area NT films can be fabricated using the approach described in this study. Annealing the NT film at 400 °C converted the NTs from the amorphous state to fully crystalline anatase TiO_2 (Figure S2a in the Supporting Information). Annealing the

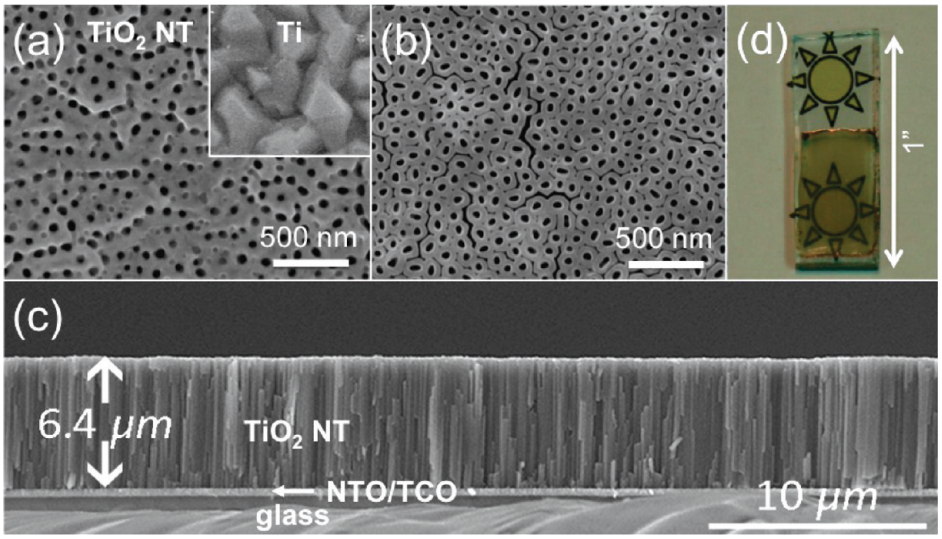

Figure 1. FE-SEM images of the as-deposited NT film (a) before and (b) after ion-beam etching and (c) a cross-sectional FE-SEM image of the NT film. The inset in (a) shows the surface of the Ti film before anodization at the same magnification used in (a) and (b). (d) Photograph of the as-deposited transparent NT film on a NTO/TCO substrate.

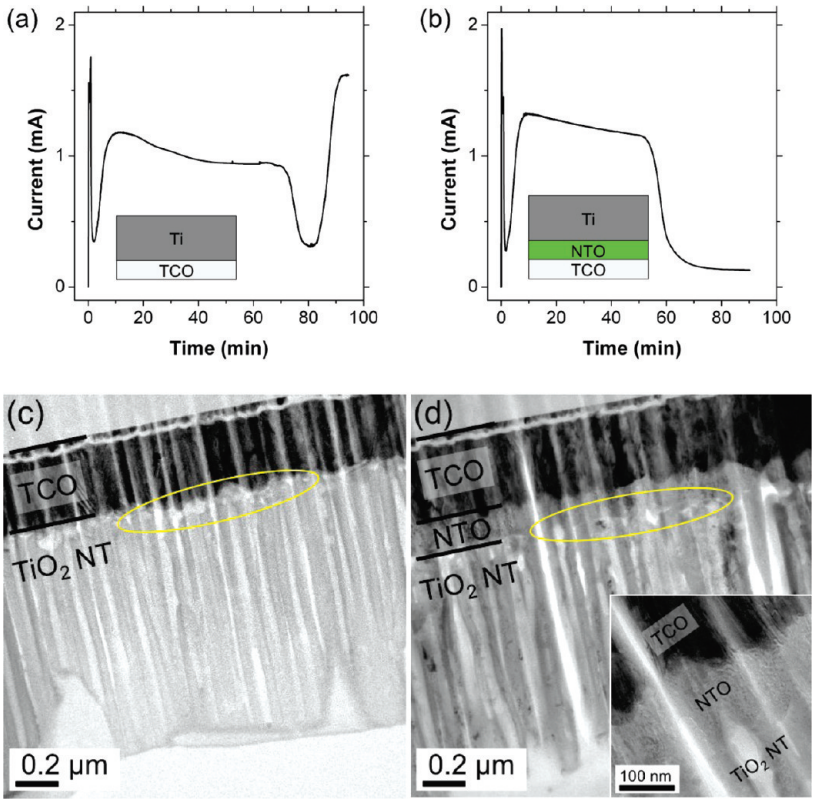

Figure 2. Current−time profiles for the anodization of Ti films (a) without and (b) with the NTO layer on the TCO substrate. Insets show the schematic structure of each sample before anodization. Cross-sectional TEM images of the transparent NT films (c) without and (d) with the NTO layer. The inset in (d) shows a magnified image of the TCO/NTO/TiO_2 NT interfaces.

film at temperatures as high as 590 °C showed no evidence of the rutile phase (Figure S2b in the Supporting Information), indicating the Ti layer was fully converted to the oxide after completion of the anodization process.[26]

Figure 2 shows the current profiles for the anodization of Ti films in the absence and in the presence of an NTO layer. The current profiles of both samples in Figure 2a,b show an initial sharp current rise at the beginning of the anodization process (<1 min), resulting from the voltage ramp. When the applied potential reaches the final anodization potential for Ti (50 V, the second peak in the current profile), the current declines precipitously and then partially recovers within the first

10 min. This current drop and subsequent recovery concur with previous observations.[21,29,30] Over the next 40−60 min, the current gradually decreases until the end of the anodization process, when it falls quickly again. During this second current drop, the NT film becomes progressively transparent, which is associated with the complete conversion of the Ti layer to the TiO_x phase. Although two samples exhibit similar current profiles up to the second current drop, subsequent events associated with continued anodization differ substantially. For samples without the NTO layer (Figure 2a), the current increases rapidly again after the second current drop followed by copious gas evolution from the electrode surface along with eventual detachment of the NT film from the TCO substrate. Similar current profile and phenomena have been noted by others.[31] The gas evolution is ascribed to oxidation of the electrolyte and the oxidative degradation of the TCO. In fact, we find that the sheet resistance of the TCO increases after detachment of the NT film, corresponding to a loss of electrical conductivity, which is indicative of TCO degradation. In marked contrast, for samples with the NTO layer, Figure 2b shows no change in current after the second drop in current, even some 30 min after the film became transparent. Also, there was no sign of gas evolution or peeling of the NT film from the TCO substrate. These results indicate that the presence of the NTO layer shields the TCO surface from direct contact with the electrolyte. This conclusion is supported by FE-SEM measurements of the substrate surfaces (Figure S3 in the Supporting Information).

The TEM images in Figure 2c,d provide insight into the causes of the events associated with the anodization of the Ti layer after the second current drop in Figure 2a,b. They show cross-sectional views of the interface region between a transparent as-deposited NT array and the TCO substrate (Figure 2c) and the interfaces between a transparent NT array and the NTO layer and between a NTO layer and the TCO substrate (Figure 2d). The TEM image in Figure 2c was taken of an anodized sample without the NTO layer; the sample was removed at the lowest current point immediately after the second current decline, just before gas would have begun evolving from the TCO surface. The TEM image (Figure 2c) reveals that the interfacial region between the NTs and TCO, marked by the yellow oval, appears as a hazy white mass. The relatively lighter color of this interfacial region is an indicator of either voids or a less dense oxide. This observation is consistent with the partial degradation and loss of homogeneity of the NT−TCO interface. Presumably, this leads to the creation of electronic defects and weakening of the strength of the adhesion between the NT arrays and TCO substrate. Figure 2d shows that the anodization of the sample with the NTO layer leads to an interfacial region, designated by the yellow oval, in which the NTs appear to coalesce with the NTO layer. The inset of Figure 2d indicates that the NTO layer is about 140 nm thick and covers completely the TCO surface. It also shows that the NTO is in intimate contact with the NT arrays and the TCO substrate. Even when the anodization process was extended for more than 30 min past the point where the Ti layer was completely converted to the oxide, the NTO−TCO interface displays no signs of peeling or corrosion. Having good physical contact between the TiO_2 NTs and the NTO−TCO interface would be advantageous when such arrays are used as photoelectrodes for DSSCs.

NTO Protection Mechanism. Before discussing the mechanism by which NTO protects the TCO substrate against oxidative degradation, it is worthwhile to give a brief review of the current understanding of the mechanism for NT formation. Although the mechanism for forming titanium oxide NT arrays from the electrochemical anodization of titanium is not fully understood, it is generally accepted that the formation of the oxide layer (barrier layer) and its electric field-assisted dissolution occur concomitantly and that the pore growth proceeds from the pore bottom toward the oxide−metal interface.[32,33] In fluoride-containing electrolytes, the *net ionic reactions* for the dissolution of titanium oxide[34] and the oxidation of titanium metal are described by

$$TiO_x + 6F^- \xrightarrow{\text{bias}} TiF_6^{2-} + xO^{2-} \quad (1)$$

$$Ti + xO^{2-} \xrightarrow{\text{bias}} TiO_x + 2xe^- \quad (2)$$

The electric field across the barrier layer (~50 nm)[35] at 50 V can be as high as 10^7 V/cm during steady-state anodization. Field strength of this magnitude would lead to a high local F^- ion concentration, resulting in an enhanced rate of dissolution[34] (eq 1). At the same time, the electric field would drive O^{2-} ions through the barrier layer to the oxide−metal interface,[32,33,36−38] where they would oxidize Ti metal to TiO_x (eq 2).

Once the Ti film was completely anodized and the titanium oxide barrier layer was dissolved (eq 1), the electrochemical etching solution would react with the TCO substrate, resulting in TCO degradation and gas evolution. These processes would undermine the NT film, leading to its eventual detachment as shown schematically in Figure 3a. So, what mechanism(s) allows the NTO layer to resist electrochemical etching and protect the TCO substrate during prolonged anodization of the Ti film? We find that the electrical resistivity of NTO is an important parameter.

The conductivity of NTO originates from Nb^{5+} in the Ti^{4+} matrix forming a shallow n-type donor level near the bottom of the conduction band of TiO_2.[39] The NTO conductivity can be varied by changing the Nb content or the deposition conditions. From the measurements of the sheet resistance (~2×10^5 Ω/□) and thickness (140 nm) of a sputter-deposited 10 at. % Nb-doped

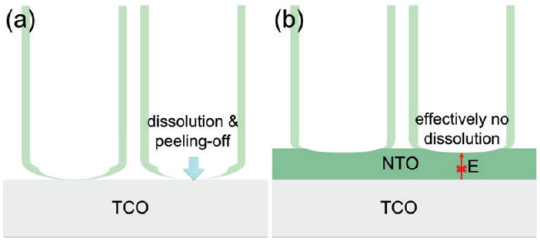

Figure 3. Schematic model of the mechanism by which the NTO layer prevents the electric field-assisted dissolution and detachment of a NT array from the TCO substrate.

TiO_2 (NTO) film on a glass substrate, we determined the electrical resistivity of the NTO layer was about 2.8 Ω·cm. From Hall-effect measurements, we confirmed that the NTO layer was n-type and determined that the electron mobility, electron concentration, and the electrical resistivity were 1.3 $cm^2/(V\ s)$, $1.4 \times 10^{18}/cm^3$, and 3.5 Ω cm, respectively. The latter value is consistent with the one obtained from the sheet resistance and film thickness (2.8 Ω cm). Because of its low electrical resistivity, the potential drop and the strength of the electric field across the NTO layer are negligible compared to those across the TiO_x layer ($\rho \approx 10^{12}$ Ω·cm for crystalline TiO_2).[40] The inappreciable strength of the electric field across the NTO layer precludes field-assisted dissolution of the NTO layer (Figure 3b). The dominant dissolution mechanism for NTO changes from a relatively fast electric field-assisted one to a purely chemical etching one, which is much slower in the electrolyte system used in the present study.[25] Viewed from another perspective, in the presence of NTO, the anodization process is self-limiting after the Ti film is completely converted to the TiO_x NT structures.

Although one might intuitively expect that a lower resistive NTO would be more effective in preventing the detachment of the NT arrays from the substrate, we find that this is not the case. We compared the electrical conductivity of NTO deposited on glass by pulsed laser deposition (PLD) and sputtering. The electrical resistivity of the sputtered NTO layer (2.8 Ω·cm) is 2 orders of magnitude higher than that of the PLD-deposited NTO layer (~0.02 Ω·cm).[41] In the case of the higher conductive PLD-deposited NTO layer, we observe both increased current and gas evolution during prolonged anodization (Figure S4b in the Supporting Information). This result suggests that when the electrical resistivity becomes too low, the oxidation of the electrolyte takes place on the conductive NTO surface. Thus, the effectiveness of the NTO layer to protect the TCO layer during the preparation of transparent TiO_2 NT arrays on TCO substrates is dependent on the extent of electrical conductivity of NTO.

Effects of the Illumination Geometry on Light-Harvesting and Charge-Collection Properties. Figure 4 shows the effect of illumination geometry at short circuit on the IPCE and charge-collection properties of a transparent DSSC constructed with a 6.4 μm thick TiO_2 NT film. The cell was probed with light incident from the electron collector (substrate) side and the counter-electrode side. Figure 4a shows that when the light is incident from the collector side, the maximum IPCE of the DSSC is 35% at 520 nm, whereas when it is incident from the counter-electrode side, the maximum IPCE of the DSSC is 13% at 545 nm, corresponding to about a 3-fold increase in IPCE for collector-side illumination. These results are qualitatively consistent with studies on the effect of illumination geometry on the conversion efficiency of NP-based DSSCs.[14,42] Furthermore, it is important to note that for counter-electrode-side illumination the IPCE is zero below 470 nm, indicating that no electrons are collected. In contrast, for collector-side illumination, electrons are collected at 350 nm and longer wavelengths (*e.g.*, the IPCE is 32% at 470 nm). To obtain a comparison of the effect of the wavelength of light on both the IPCE values and transport time constants for collector- and counter-electrode-side illumination, no white bias light was employed for the IPCE measurements. Consequently, the IPCE values in Figure 4a would underestimate the IPCE values obtained with white bias light at about 1 sun illumination intensity. The difference between the relative magnitude of the IPCE for collector- and counter-electrode-side illumination is especially pronounced in the absence of bias light (discussion associated with Figure S6a). We measure the IPCE of a DSSC with bias light at 1 sun illumination intensity (Figure S6a in Supporting Information) and find that the integrated values of the IPCE with the solar spectrum yield a short-circuit photocurrent density in good agreement with the measured J_{sc} from $J-V$ measurements (Figure S6b). Figure 4a also shows the transmittance of a sealed cell consisting of the I_3^-/I^- based redox electrolyte and TCO substrate; the optical path length between the two optical windows was the same as that for the transparent NT-based DSSCs used in this study. Essentially all wavelengths of light below 450 nm are absorbed by the redox electrolyte, which indicates that when DSSCs are illuminated through the counter-electrode side, iodide species in the electrolyte between the NT film and the counter electrode remove an appreciable fraction of the incident light before it reaches the dye-covered film. For collector-side illumination, the amount of light absorbed by the electrolyte in the nanopores of the stained films would be substantially less than that by the bulk electrolyte between the NT film and the counter electrode. These results are in accord with the dependence of the photoelectron density on illumination geometry and wavelengths of incident light at different intensities (Figure S5 in the Supporting Information).

Figure 4b compares the light absorption by dye molecules adsorbed to the surface of the NTs and the normalized IPCE spectrum for a DSSC subjected to counter-electrode-side illumination. The amount of light

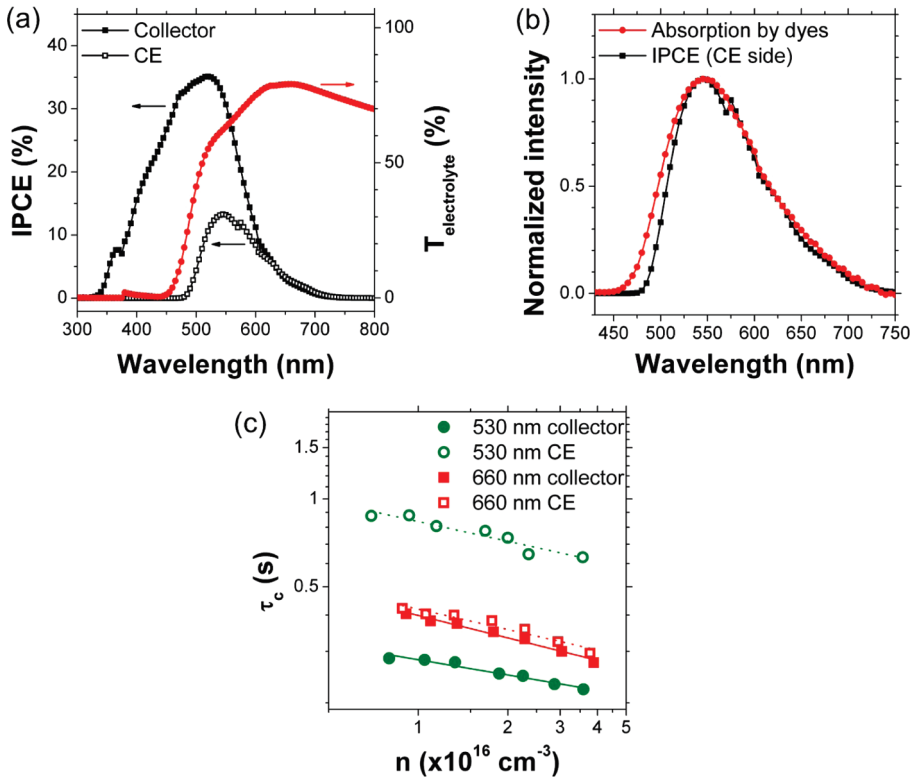

Figure 4. (a) IPCE spectra of a transparent NT-based DSSC illuminated from the collector side and counter-electrode side, and transmittance spectrum of the electrolyte containing the iodide electrolyte; (b) normalized IPCE spectrum of a DSSC illuminated from the counter-electrode side and the normalized net absorption spectrum of dye molecules adsorbed to a TiO_2 NT film; (c) transport time constants at short circuit for the DSSC as a function of the photoelectron density for the collector-side and counter-electrode-side illumination with 530 and 660 nm light pulses; lines are best fit of the data.

absorbed by the redox electrolyte, TiO_2 NT film, and TCO substrate was subtracted from the absorption spectra.[43] Thus, the light absorption spectrum represents the absorption spectrum of just the adsorbed dye. The IPCE and absorption spectra were normalized with respect to their maximum values at 545 nm. Figure 4b shows that IPCE values at wavelengths shorter than 545 nm are significantly less than the absorbed light by the dye. Moreover, the IPCE onset is shifted 30 nm to longer wavelengths with respect to the onset for light absorption, indicating that a significant fraction of absorbed photons does not contribute to the photoresponse of the cell. The IPCE (or, equivalently, the external quantum efficiency) is the product of light-harvesting, charge-injection, and charge-collection efficiencies. The short-circuit photocurrent is proportional to the IPCE ($J_{sc} \propto$ IPCE). The difference in IPCE and light absorption spectra at wavelengths < 545 nm (Figure 4b) cannot be attributed to the charge-injection efficiency, which is expected to increase with higher excitation energies.[44,45] This result implies that a significant fraction of the photoinjected electrons (*e.g.*, *ca.* 25% at 490 nm), which are generated by the absorption of higher energy photons (<545 nm), recombine with the redox electrolyte before being collected, suggesting that the loss of charge-collection efficiency lowers the IPCE. These results (Figure 4a,b) are in accord with the dependence of the photoelectron density on illumination geometry and wavelengths of incident light at different intensities (Figure S4 in the Supporting Information).

Figure 4c compares transport time constants (τ_c) at short circuit for transparent NT-based DSSC as a function of the photoelectron density (n) for collector- and counter-electrode-side illumination. The transport time constants exhibit the usual power-law dependency on n, regardless of the wavelength of the incident light and illumination geometry. The power-law dependence of transport has been explained by a model in which electrons perform an exclusive random walk between trap sites that have a power-law distribution of waiting (release) times in the form of $t^{-1-\alpha}$, where parameter α is in the range from 0 to 1 and can be related to the shape of the trap distribution.[15,46] The best fit of the data yields parallel lines independent of the illumination wavelength and geometry, indicating that the density and distribution of transport-limiting traps are uniform across the NT films. When the cell is illuminated with a 530 nm light pulse incident from the collector side, the transport times are shorter than when incident from the counter-electrode side. For example, at the same photoelectron density ($n = 2 \times 10^{16}$ cm^{-3}), the transport time for collector-side illumination (τ_c = 0.25 s) is about 3 times faster than the

transport time for counter-electrode-side illumination ($\tau_c = 0.72$ s). When the cell is illuminated with a 660 nm light pulse incident from either the collector or counter-electrode side, the transport times ($\tau_c = 0.35$ s) are the same (within 10% of experimental error). The wavelength dependence of the time constants can be understood in terms of the spatial distribution and temporal relationship between the absorption profile and the arrival time of electrons at the electron-collecting electrode. Because of the strong absorption of the 530 nm light pulse by the dye (the effective absorption coefficient of the cell $\varepsilon \approx 2500$ cm^{-1} for 530 nm light), the injected electrons are introduced into a relatively narrow spatial region of the film, corresponding to where the light pulse enters the film. The transport time will depend, therefore, on the average distance that injected electrons travel to reach the collecting electrode. The average distance d_{av} that an electron would travel for the 530 and 660 nm light pulses can be estimated from the respective light absorption profile *via* the expression $d_{av} = \int_0^L x e^{-\varepsilon x}\, dx / \int_0^L e^{-\varepsilon x}\, dx$ where ε is the absorption coefficient and L is film thickness. Therefore, when the 530 nm light pulse enters the cell from the counter-electrode side, the bulk of injected electrons are produced relatively near the outermost surface of the NT film and must travel on average a distance of about 4 μm through the 6.4 μm thick NT films before being collected at the TCO substrate. In contrast, electrons that are created near the TCO substrate, as in the case where the 530 nm light pulse enters the cell at the TCO substrate, have a shorter distance to travel (*ca.* 2.4 μm) before being collected. On the other hand, the 660 nm light is relatively weakly absorbed by the dye (the effective absorption coefficient of the cell $\varepsilon \approx 500$ cm^{-1} for 660 nm light) and therefore produces a relatively constant electron injection current across the film. Thus, when the 660 nm light pulse enters the cell from either the collector or counter-electrode side, the bulk of the injected electrons are produced relatively uniformly throughout the film and must travel roughly the same distance on average, about 3.2 μm, before being collected at the TCO substrate. From the values for the average distance an electron travels through a film d_{av} and the transport time constant τ_c, one can estimate the electron diffusion coefficient from the expression $D_n = d_{av}^2/2.35\tau_c$.[15,47] At a constant photoelectron density ($n = 2 \times 10^{16}$ cm^{-3}), the electron diffusion coefficient for collector- and counter-electrode-side illumination is the same, about 10^{-7} cm^{-2}/s, regardless of the wavelength of light.

Solar Cell Performance. Figure 5 and Table 1 show the effect of illumination direction on the photocurrent density–voltage (J–V) characteristics of transparent TiO_2 NT-based DSSCs. No effort was made to optimize the DSSC performance. Photocurrent densities of the DSSC with the 6.4 μm thick film were 88% larger for collector-side illumination than for counter-electrode-side illumination,

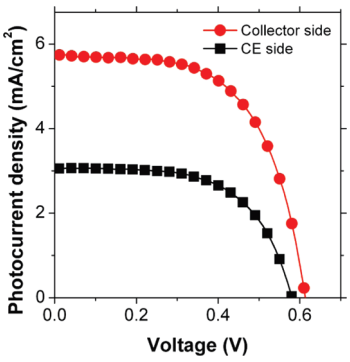

Figure 5. J–V characteristics of a transparent TiO_2 NT-based DSSC illuminated from the collector side and counter-electrode side under simulated AM 1.5 light; the NT film was 6.4 μm thick.

TABLE 1. J–V Characteristics of Transparent TiO_2 NT-Based DSSCs with Different Film Thicknesses

illumination direction	film thickness (μm)	J_{sc} (mA/cm^2)	V_{oc} (V)	FF	η (%)
collector side	6.4	5.74	0.61	0.60	2.11
counter-electrode side	6.4	3.05	0.58	0.60	1.07
collector side	13[a]	8.35	0.70	0.72	4.19
counter-electrode side	13[a]	6.75	0.68	0.65	2.99

[a] Figure S6b in the Supporting Information.

while the illumination geometry dependence of the open-circuit photovoltage (V_{oc}) and the fill factor (FF) was much less. From IPCE and transmittance measurements, we conclude that the major cause for the lower photocurrent density for counter-electrode-side illumination is the attenuation of the incident light with wavelengths below 470 nm by the redox electrolyte (Figure 4a and S6). The loss of photoelectron density resulting from recombination (Figure 4b,c) should also lower photocurrent density for counter-electrode-side illumination. The loss due to recombination for the counter-electrode-side illumination was estimated using the expression $\int[\mathrm{IPCE}(\lambda)/\mathrm{LHE}(\lambda)] \cdot \Phi(\lambda)\, d\lambda / \int \Phi(\lambda)\, d\lambda$, where $\Phi(\lambda)$ is the AM 1.5 energy spectrum and LHE is the light-harvesting efficiency corresponding to the net absorption spectrum of the dye-covered NT film (Figure 4b). From the analysis of IPCE and absorption spectra, we calculated that the recombination loss was about 14%, corresponding to 14% loss in J_{sc} over the solar spectrum. From the perspective of *collector-side* illumination, we estimate that, of the observed 88% gain in J_{sc}, 74% of that gain was due to increased light absorption by the dye and 14% of it resulted from reduced recombination. However, changing the optical path length through a cell would alter the contributions of both light absorption and recombination to J_{sc} and to the cell conversion efficiency. Decreasing the optical path length should reduce the light-absorption contribution and increase the recombination contribution, the consequence of which would be to reduce the difference between the photocurrent densities (and conversion efficiencies) for collector-side

and counter-electrode-side illumination. Increasing the optical length should have the opposite effect. Perhaps surprisingly, the photovoltage of the cell showed only a small dependence on the illumination direction in spite of the loss of photocurrent density for counter-electrode-side illumination. For collector-side illumination, the gain in V_{oc} was only 30 mV, representing a 5% improvement over that for the counter-electrode illumination. The small improvement in V_{oc} is understandable inasmuch as it depends logarithmically on the photocurrent density ($V_{oc} = (\beta kT/q) \ln(J_{sc}/J_0)$, where β is the diode ideality factor, k is the Boltzmann constant, T is the temperature, and J_0 is the dark exchange current)[48] and, thus, is only weakly dependent on changes in photocurrent density. Assuming a β value of 1.9, we calculate a 30 mV increase for collector-side illumination in concurrence with the measured value. The 30 mV increase in V_{oc} derives from the larger photoelectron density ($V_{oc} \propto \ln(n)$),[12,48] resulting from the greater amount of light absorbed and the reduced recombination for collector-side illumination (Figure 4). The fill factors display little dependence on the illumination direction because the ohmic drop across the cell associated with the photocurrent compensates the shunt resistance associated with recombination. For example, for collector-side illumination, a higher J_{sc} should lead to a larger ohmic drop, but at the same time a smaller shunt resistance should compensate this effect. Thus, the change in the photocurrent density resulting from the dependence of the light-harvesting efficiency on the illumination direction is the main determinant of the solar conversion efficiency. The net effect of the various changes in J_{sc}, V_{oc}, and the fill factor is that the cell efficiency was 97% higher for collector-side illumination than for counter-electrode-side illumination. Similar results were obtained when the thickness of the NT film was increased from 6.4 to 13 μm, although the solar conversion efficiency almost doubled, jumping to 4.2% from 2.1% (Figure S6 in the Supporting Information).

CONCLUSIONS

In summary, we demonstrated a general approach for preparing transparent anatase TiO_2 NT arrays onto transparent conducting oxide (TCO) substrates. By employing a conducting Nb-doped TiO_2 (NTO) layer between Ti film and TCO, the Ti metal film can be anodized completely without degrading the TCO and NT array, even after a prolonged period of anodization. The NTO layer was shown to protect the TCO against degradation through a self-terminating mechanism by essentially arresting the electric field-assisted dissolution process at the NT−NTO interface. The conductivity of the NTO was found to be a critical parameter in preventing further anodization. Without the protective (conducting) NTO layer, prolonged anodization led to the electrochemical corrosion of the TCO layer and detachment of the NT film from the TCO substrate. After prolonged anodization, the NTO layer was still strongly bonded to the NT array and to the TCO substrate, resulting in a transparent NT arrays without residual Ti. Furthermore, annealing of the as-prepared NT film at temperatures as high as 590 °C showed no trace of the rutile phase, confirming that the Ti metal layer was converted to the oxide after completion of the anodization process. Illumination geometry was found to strongly alter the transport times of electrons, IPCE, and photoelectrochemical properties of the DSSCs. The solar conversion efficiency of the cell was about 2 times higher for collector-side illumination than for counter-electrode-side illumination. The higher conversion efficiency was mainly due to a larger photocurrent density associated with the higher light-harvesting efficiency of the cell. A decrease in recombination for collector-side illumination also contributed to the high conversion efficiency although to a much lesser extent. It is noteworthy, however, that changing the optical path length through a cell would be expected to alter the contributions of both light absorption and recombination to J_{sc} and to the cell conversion efficiency. On the other hand, the open-circuit photovoltage displayed only a weak dependence on the illumination geometry. Similar results were obtained when the NT film thickness was increased by about 2-fold, one consequence of which was the doubling of the solar conversion efficiency. The electrochemical strategy described in this study will find important usage in the fabrication of transparent NT array electrodes for solar energy conversion and other optoelectronic applications.

METHODS

The transparent TiO_2 NT arrays were prepared as follows: 10 at. % Nb-doped TiO_2 (NTO) thin layers were deposited on fluorine-doped SnO_2 conducting glass (TCO, Pilkington TEC15) substrates by rf-magnetron sputtering using a Nb-doped TiO_2 target at 400 °C under Ar flow (20 sccm) with a working pressure of 5 mTorr. Titanium films were deposited on top of the NTO layer by rf-magnetron sputtering using a Ti target (99.9%) under the same sputtering conditions used for the NTO deposition. The thickness of the Ti films was normally about 2.4 μm. For the thickest NT films, the Ti film thickness was 5 μm. The aligned NT arrays were produced by electrochemically anodizing the Ti films at 50 V (ramping rate; 1 V/s) in a two-electrode cell, which contained a Pt counter electrode and 0.25 wt % NH_4F (99.9%) in ethylene glycol (99%) with 1 wt % added H_2O; the composition of the solution was adapted from the literature.[49] A computer-controlled source meter was used for the electrochemical anodization. The as-prepared samples were rinsed with water, followed by ethanol, and then dried under a stream of nitrogen.

Next, the pores of the NT films were widened by immersing the films for 5 min in a formamide solution containing 0.15 M NH_4F and 3.5 wt % H_2O at 80 °C followed by the same rinsing and drying sequence noted above. After they were annealed at 400 °C for 1 h in air, the TiO_2 NT arrays were soaked in aqueous 0.05 M $TiCl_4$ solution at 70 °C for 30 min and then rinsed and dried using the same process used above. A second annealing of the films at 400 °C in air for 30 min followed, and the resulting anatase films were immersed in 0.3 mM Z907 dye (Z907 = *cis*-bis(isothiocyanato)(2,2′-bipyridyl-4,4′-dicarboxylato)(4,4′-dinonyl-2′-bipyridyl)ruthenium(II)) in a acetonitrile and *tert*-butyl alcohol solution (1:1 v/v) and then assembled into DSSCs as detailed before.[13] The DSSCs were sealed with two layers of Surlyn thermoplastic, each 20 μm thick. The cells were filled with an electrolyte composed of 1.0 M 1-methyl-3-propylimidazolium iodide (PMII), 30 mM iodine, 0.5 M 1-butyl-1*H*-benzimidazole (NBB), and 0.1 M guanidinium thiocyanate (GuNCS) in 3-methoxypropionitrile (MPN).[50]

The sheet resistances of NTO layers, deposited on fused silica glass substrates, were determined by the four-point probe technique. The thickness of the NTO layer was determined by field-emission scanning electron microscopy and confirmed using a surface profiler. The electrical resistivity of the NTO layer was determined from the sheet resistance and film thickness and from Hall-effect measurements. The morphological properties of NT films were characterized by FE-SEM with energy dispersive X-ray spectroscopy, high-resolution transmission electron microscopy, and X-ray diffraction, respectively. The optical absorption/transmission spectra and external quantum efficiencies were obtained with an IPCE measurement system. The transport time constants and photoelectron densities were measured by time-of-flight. Pulses of 530 or 660 nm wavelength light from light-emitting diodes were incident on the cell from either the TiO_2 NT film side or the electrolyte side. The pulse width was about 20 μs. The intensity of the incident light pulses was controlled using neutral density filters. The TOF current response was amplified using a current preamplifier and recorded using a digitizing oscilloscope. Current transients were collected for long enough times that the integrated charge-collection transient was saturated. The setup for determining characteristics of DSSCs under simulated AM 1.5 solar irradiance is discussed elsewhere.[51]

Acknowledgment. This work was supported by the Division of Chemical Sciences, Geosciences, and Biosciences, Office of Basic Energy Sciences (A.F.H., A.J.F.), and the Division of Photovoltaics, Office of Utility Technologies, (J.Y.K., K Z., N.R.N.), U.S. Department of Energy, under contract no. DE-AC36-08GO28308.

Supporting Information Available: FE-SEM images of Ti film used in preparing 13 μm thick titania NT film, TCO and NTO/TCO substrates after prolonged anodization of Ti layers, and surface morphology of Ti films deposited at different temperatures; anodization current profile of a Ti film with NTO layer deposited by PLD; XRD patterns of a NT film before and after thermal annealing; dependence of photoelectron density on wavelength of light pulses for collector-side and counter-electrode-side illumination; comparison of IPCE spectra and $J-V$ characteristics of TiO_2 NT-based DSSC with a 13 μm thick film for different illumination geometries. This material is available free of charge *via* the Internet at http://pubs.acs.org.

REFERENCES AND NOTES

1. Macak, J. M.; Tsuchiya, H.; Ghicov, A.; Schmuki, P. Dye-Sensitized Anodic TiO_2 Nanotubes. *Electrochem. Commun.* **2005,** *7*, 1133–1137.
2. Baker, D. R.; Kamat, P. V. Photosensitization of TiO_2 Nanostructures with CdS Quantum Dots: Particulate versus Tubular Support Architectures. *Adv. Funct. Mater.* **2009,** *19*, 805–811.
3. Park, J. H.; Kim, S.; Bard, A. J. Novel Carbon-Doped TiO_2 Nanotube Arrays with High Aspect Ratios for Efficient Solar Water Splitting. *Nano Lett.* **2006,** *6*, 24–28.
4. Varghese, O. K.; Paulose, M.; LaTempa, T. J.; Grimes, C. A. High-Rate Solar Photocatalytic Conversion of CO_2 and Water Vapor to Hydrocarbon Fuels. *Nano Lett.* **2009,** *9*, 731–737.
5. Nah, Y. C.; Ghicov, A.; Kim, D.; Berger, S.; Schmuki, P. TiO_2-WO_3 Composite Nanotubes by Alloy Anodization: Growth and Enhanced Electrochromic Properties. *J. Am. Chem. Soc.* **2008,** *130*, 16154–16155.
6. Liu, S. Q.; Fang, D.; Li, Z. J.; Huang, K. L. Fabrication and Fluorescence Property of Titanium Dioxide Nanotube Arrays by Anodizing Processes. *Chin. J. Inorg. Chem.* **2007,** *23*, 827–832.
7. Varghese, O. K.; Gong, D. W.; Paulose, M.; Ong, K. G.; Grimes, C. A. Hydrogen Sensing Using Titania Nanotubes. *Sens. Actuators, B* **2003,** *93*, 338–344.
8. Banerjee, S.; Mohapatra, S. K.; Misra, M.; Mishra, I. B. The Detection of Improvised Nonmilitary Peroxide-Based Explosives Using a Titania Nanotube Array Sensor. *Nanotechnology* **2009,** *20*, 075502.
9. Zheng, Q.; Zhou, B.; Bai, J.; Li, L.; Jin, Z.; Zhang, J.; Li, J.; Liu, Y.; Cai, W.; Zhu, X. Self-Organized TiO_2 Nanotube Array Sensor for the Determination of Chemical Oxygen Demand. *Adv. Mater.* **2008,** *20*, 1044–1049.
10. Kuang, D.; Brillet, J.; Chen, P.; Takata, M.; Uchida, S.; Miura, H.; Sumioka, K.; Zakeeruddin, S. M.; Grätzel, M. Application of Highly Ordered TiO_2 Nanotube Arrays in Flexible Dye-Sensitized Solar Cells. *ACS Nano* **2008,** *2*, 1113–1116.
11. Zhu, K.; Vinzant, T. B.; Neale, N. R.; Frank, A. J. Removing Structural Disorder from Oriented TiO_2 Nanotube Arrays: Reducing the Dimensionality of Transport and Recombination in Dye-Sensitized Solar Cells. *Nano Lett.* **2007,** *7*, 3739–3746.
12. Liu, Z. L.; Misra, M. Dye-Sensitized Photovoltaic Wires Using Highly Ordered TiO_2 Nanotube Arrays. *ACS Nano* **2010,** *4*, 2196–2200.
13. Jennings, J. R.; Ghicov, A.; Peter, L. M.; Schmuki, P.; Walker, A. B. Dye-Sensitized Solar Cells Based on Oriented TiO_2 Nanotube Arrays: Transport, Trapping, and Transfer of Electrons. *J. Am. Chem. Soc.* **2008,** *130*, 13364–13372.
14. Ito, S.; Ha, N. L. C.; Rothenberger, G.; Liska, P.; Comte, P.; Zakeeruddin, S. M.; Pechy, P.; Nazeeruddin, M. K.; Grätzel, M. High-Efficiency (7.2%) Flexible Dye-Sensitized Solar Cells with Ti-Metal Substrate for Nanocrystalline-TiO_2 Photoanode. *Chem. Commun.* **2006,** 4004–4006.
15. van de Lagemaat, J.; Frank, A. J. Nonthermalized Electron Transport in Dye-Sensitized Nanocrystalline TiO_2 Films: Transient Photocurrent and Random-Walk Modeling Studies. *J. Phys. Chem. B* **2001,** *105*, 11194–11205.
16. Zhu, K.; Neale, N. R.; Miedaner, A.; Frank, A. J. Enhanced Charge-Collection Efficiencies and Light Scattering in Dye-Sensitized Solar Cells Using Oriented TiO_2 Nanotubes Arrays. *Nano Lett.* **2007,** *7*, 69–74.
17. Yum, J.-H.; Chen, P.; Grätzel, M.; Nazeeruddin, M. K. Recent Developments in Solid-State Dye-Sensitized Solar Cells. *ChemSusChem* **2008,** *1*, 699–707.
18. Leschkies, K. S.; Jacobs, A. G.; Norris, D. J.; Aydil, E. S. Nanowire-Quantum-Dot Solar Cells and the Influence of Nanowire Length on the Charge Collection Efficiency. *Appl. Phys. Lett.* **2009,** *95*, 193103.
19. Pattantyus-Abraham, A. G.; Kramer, I. J.; Barkhouse, A. R.; Wang, X.; Konstantatos, G.; Debnath, R.; Levina, L.; Raabe, I.; Nazeeruddin, M. K.; Grätzel, M.; *et al*. Depleted-Heterojunction Colloidal Quantum Dot Solar Cells. *ACS Nano* **2010,** *4*, 3374–3380.
20. Mor, G. K.; Kim, S.; Paulose, M.; Varghese, O. K.; Shankar, K.; Basham, J.; Grimes, C. A. Visible to Near-Infrared Light Harvesting in TiO_2 Nanotube Array-P3HT Based Heterojunction Solar Cells. *Nano Lett.* **2009,** *9*, 4250–4257.
21. Mor, G. K.; Varghese, O. K.; Paulose, M.; Grimes, C. A. Transparent Highly Ordered TiO_2 Nanotube Arrays *via* Anodization of Titanium Thin Films. *Adv. Funct. Mater.* **2005,** *15*, 1291–1296.
22. Ghicov, A.; Alba, S. P.; Macak, J. M.; Schmuki, P. High-Contrast Electrochromic Switching Using Transparent Lift-off Layers of Self-Organized TiO_2 Nanotubes. *Small* **2008,** *4*, 1063–1066.

23. Mor, G. K.; Shankar, K.; Paulose, M.; Varghese, O. K.; Grimes, C. A. Use of Highly-Ordered TiO_2 Nanotube Arrays in Dye-Sensitized Solar Cells. *Nano Lett.* **2006,** *6*, 215–218.
24. Sadek, A. Z.; Zheng, H.; Latham, K.; Wlodarski, W.; Kalantarzadeh, K. Anodization of Ti Thin Film Deposited on ITO. *Langmuir* **2008,** *25*, 509–514.
25. Varghese, O. K.; Paulose, M.; Grimes, C. A. Long Vertically Aligned Titania Nanotubes on Transparent Conducting Oxide for Highly Efficient Solar Cells. *Nat. Nanotechnol.* **2009,** *4*, 592–597.
26. Zhu, K.; Neale, N. R.; Halverson, A. F.; Kim, J. Y.; Frank, A. J. Effects of Annealing Temperature on the Charge-Collection and Light-Harvesting Properties of TiO_2 Nanotube-Based Dye-Sensitized Solar Cells. *J. Phys. Chem. C* **2010,** *114*, 13433–13441.
27. Varghese, O. K.; Gong, D. W.; Paulose, M.; Grimes, C. A.; Dickey, E. C. Crystallization and High-Temperature Structural Stability of Titanium Oxide Nanotube Arrays. *J. Mater. Res.* **2003,** *18*, 156–165.
28. Wang, D.; Liu, Y.; Yu, B.; Zhou, F.; Liu, W. TiO_2 Nanotubes with Tunable Morphology, Diameter, and Length: Synthesis and Photo-Electrical/Catalytic Performance. *Chem. Mater.* **2009,** *21*, 1198–1206.
29. Shin, Y.; Lee, S. Self-Organized Regular Arrays of Anodic TiO_2 Nanotubes. *Nano Lett.* **2008,** *8*, 3171–3173.
30. Albu, S. P.; Kim, D.; Schmuki, P. Growth of Aligned TiO_2 Bamboo-Type Nanotubes and Highly Ordered Nanolace. *Angew. Chem., Int. Ed.* **2008,** *47*, 1916–1919.
31. Berger, S.; Ghicov, A.; Nah, Y. C.; Schmuki, P. Transparent TiO_2 Nanotube Electrodes *via* Thin Layer Anodization: Fabrication and Use in Electrochromic Devices. *Langmuir* **2009,** *25*, 4841–4844.
32. Mor, G. K.; Varghese, O. K.; Paulose, M.; Shankar, K.; Grimes, C. A. A Review on Highly Ordered, Vertically Oriented TiO_2 Nanotube Arrays: Fabrication, Material Properties, and Solar Energy Applications. *Sol. Energy Mater. Sol. Cells* **2006,** *90*, 2011–2075.
33. Macak, J. M.; Tsuchiya, H.; Ghicov, A.; Yasuda, K.; Hahn, R.; Bauer, S.; Schmuki, P. TiO_2 Nanotubes: Self-Organized Electrochemical Formation, Properties and Applications. *Curr. Opin. Solid State Mater. Sci.* **2007,** *11*, 3–18.
34. Bright, E.; Readey, D. W. Dissolution Kinetics of TiO_2 in HF-HCl Solutions. *J. Am. Ceram. Soc.* **1987,** *70*, 900–906.
35. Macak, J. M.; Tsuchiya, H.; Taveira, L.; Aldabergerova, S.; Schmuki, P. Smooth Anodic TiO_2 Nanotubes. *Angew. Chem., Int. Ed.* **2005,** *44*, 7463–7465.
36. O'Sullivan, J. P.; Wood, G. C. The Morphology and Mechanism of Formation of Porous Anodic Films on Aluminium. *Proc. R. Soc. A* **1970,** *317*, 511–543.
37. Jessensky, O.; Muller, F.; Gösele, U. Self-Organized Formation of Hexagonal Pore Arrays in Anodic Alumina. *Appl. Phys. Lett.* **1998,** *72*, 1173–1175.
38. Parkhutik, V. P.; Shershulsky, V. I. Theoretical Modeling of Porous Oxide-Growth on Aluminum. *J. Phys. D: Appl. Phys.* **1992,** *25*, 1258–1263.
39. Furubayashi, Y.; Hitosugi, T.; Yamamoto, Y.; Inaba, K.; Kinoda, G.; Hirose, Y.; Shimada, T.; Hasegawa, T. A Transparent Metal: Nb-doped Anatase TiO_2. *Appl. Phys. Lett.* **2005,** *86*, 252101.
40. Earle, M. D. The Electrical Conductivity of Titanium Dioxide. *Phys. Rev.* **1942,** *61*, 56–62.
41. Noh, J. H.; Lee, S.; Kim, J. Y.; Lee, J. K.; Han, H. S.; Cho, C. M.; Cho, I. S.; Jung, H. S.; Hong, K. S. Functional Multilayered Transparent Conducting Oxide Thin Films for Photovoltaic Devices. *J. Phys. Chem. C* **2009,** *113*, 1083–1087.
42. Lee, S.; Noh, J. H.; Han, H. S.; Yim, D. K.; Kim, D. H.; Lee, J. K.; Kim, J. Y.; Jung, H. S.; Hong, K. S. Nb-Doped TiO_2: A New Compact Layer Material for TiO_2 Dye-Sensitized Solar Cells. *J. Phys. Chem. C* **2009,** *113*, 6878–6882.
43. The net absorption spectrum by dye molecules was calculated by subtracting the absorption spectrum of the cell with the dye from one without the dye.
44. Liu, F.; Meyer, G. J. Excited State Interfacial Electron Transfer from a Compound with a Single Pyridine Ligand. *Inorg. Chem.* **2003,** *42*, 7351–7353.
45. Asbury, J. B.; Anderson, N. A.; Hao, E.; Ai, X.; Lian, T. Parameters Affecting Electron Injection Dynamics from Ruthenium Dyes to Titanium Dioxide Nanocrystalline Thin Film. *J. Phys. Chem. B* **2003,** *107*, 7376–7386.
46. Nelson, J.; Haque, S. A.; Klug, D. R.; Durrant, J. R. Trap-Limited Recombination in Dye-Sensitized Nanocrystalline Metal Oxide Electrodes. *Phys. Rev. B* **2001,** *63*, 205321.
47. Zhu, K.; Kopidakis, N.; Neale, N. R.; van de Lagemaat, J.; Frank, A. J. Influence of Surface Area on Charge Transport and Recombination in Dye-Sensitized TiO_2 Solar Cells. *J. Phys. Chem. B* **2006,** *110*, 25174–25180.
48. Frank, A. J.; Kopidakis, N.; van de Lagemaat, J. Electrons in Nanostructured TiO_2 Solar Cells: Transport, Recombination and Photovoltaic Properties. *Coord. Chem. Rev.* **2004,** *248*, 1165–1179.
49. Paulose, M.; Shankar, K.; Yoriya, S.; Prakasam, H. E.; Varghese, O. K.; Mor, G. K.; Latempa, T. A.; Fitzgerald, A.; Grimes, C. A. Anodic Growth of Highly Ordered TiO_2 Nanotube Arrays to 134 μm in Length. *J. Phys. Chem. B* **2006,** *110*, 16179–16184.
50. Kuang, D.; Klein, C.; Ito, S.; Moser, J.-E.; Humphry-Baker, R.; Evans, N.; Duriaux, F.; Grätzel, C.; Zakeeruddin, S. M.; Grätzel, M. High-Efficiency and Stable Mesoscopic Dye-Sensitized Solar Cells Based on a High Molar Extinction Coefficient Ruthenium Sensitizer and Nonvolatile Electrolyte. *Adv. Mater.* **2007,** *19*, 1133–1137.
51. Neale, N. R.; Kopidakis, N.; van de Lagemaat, J.; Grätzel, M.; Frank, A. J. Effect of a Coadsorbent on the Performance of Dye-Sensitized TiO_2 Solar Cells: Shielding versus Band-Edge Movement. *J. Phys. Chem. B* **2005,** *109*, 23183–23189.